

SMUDLP: Self-Teaching Multi-Frame Unsupervised Endoscopic Depth Estimation with Learnable Patchmatch

Shuwei Shao, Zhongcai Pei, Weihai Chen, Xingming Wu, Zhong Liu, Zhengguo Li

Abstract—Unsupervised monocular trained depth estimation models make use of adjacent frames as a supervisory signal during the training phase. However, temporally correlated frames are also available at inference time for many clinical applications, *e.g.*, surgical navigation. The vast majority of monocular systems do not exploit this valuable signal that could be deployed to enhance the depth estimates. Those that do, achieve only limited gains due to the unique challenges in endoscopic scenes, such as low and homogeneous textures and inter-frame brightness fluctuations. In this work, we present SMUDLP, a novel and unsupervised paradigm for multi-frame monocular endoscopic depth estimation. The SMUDLP integrates a learnable patchmatch module to adaptively increase the discriminative ability in low-texture and homogeneous-texture regions, and enforces cross-teaching and self-teaching consistencies to provide efficacious regularizations towards brightness fluctuations. Our detailed experiments on both SCARED and Hamlyn datasets indicate that the SMUDLP exceeds state-of-the-art competitors by a large margin, including those that use single or multiple frames at inference time. The source code and trained models will be publicly available upon the acceptance.

Index Terms—Unsupervised learning, Multi-frame depth estimation, Learnable patchmatch, Cross-teaching, Self-teaching

I. INTRODUCTION

Monocular depth estimation has shown to be a practical and versatile technology with a variety of applications, such as simultaneously localization and mapping (SLAM) [1], surgical navigation [2] and augmented reality [3]. While hardware sensors, *e.g.*, structured light, are capable of capturing depth range, the specialist hardware fails to collect dense depth maps and using only one single RGB camera is a more promising approach due to its low cost. Many recent methods frame the monocular depth from RGB as a task of novel view synthesis, which eliminates the limitation of costly hardware sensors to acquire training depth data [4]–[7]. However, the depth estimation accuracy is still far from satisfactory yet.

In this work, we argue that in most real-world scenarios, for instance, surgical navigation, more than one frame is available at inference time, and that the additional frames are valuable and should be exploited by the monocular depth estimation

This work was supported by the Key Research and Development Program of Shandong Province under Grant NO.2019JZZY011101.

Shuwei Shao, Zhongcai Pei, Weihai Chen, Xingming Wu and Zhong Liu are with the School of Automation Science and Electrical Engineering, Beihang University, Beijing, China. (email: swshao@buaa.edu.cn, peizc@buaa.edu.cn, whchen@buaa.edu.cn, xmwubuaa@163.com, Liuzhong@buaa.edu.cn)

Zhengguo Li is with the SRO department, Institute for Infocomm Research, 1 Fusionopolis Way, Singapore. (ezgli@i2r.a-star.edu.sg)
corresponding author: Weihai Chen

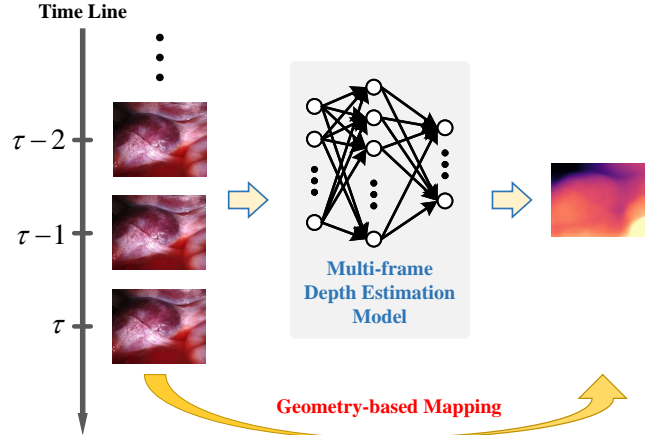


Fig. 1. Our method, which trains and tests on endoscopic video streams rather than isolated images, produces accurate depth estimates.

to a better practice. Unfortunately, based on our observations and experiments, the real strengths of the unsupervised multi-frame depth estimation model are hidden for several reasons (Fig. 2). First, the overall scarce and homogeneous textures of tissues are observed in endoscopy, which makes it hard for the model to obtain reliable information from photometric error¹. For example, the predicted depth may be incorrect up to infinite, while the photometric error still displays a low value. Second, the brightness constancy assumption is not available in endoscopy. The inter-frame illumination of the same anatomy varies substantially when the camera and light source move through the environments. In addition, strong non-Lambertian reflections and inter-reflections are caused in the surfaces of smooth tissues and organ fluids. In such regions, photometric error and cost volume² are susceptible to be confused by the severe brightness fluctuations. To overcome the challenges, we introduce several innovations: (i) a **learnable patchmatch module** to induce a more distinctive characterization in low-texture and homogeneous-texture regions by adaptive propagation; (ii) **cross-teaching and self-teaching paradigms** to enhance the robustness towards severe brightness fluctuations. We refer to the resultant multi-frame monocular system *Self-Teaching Multi-Frame Unsupervised Endoscopic Depth Estimation with Learnable Patchmatch* as **SMUDLP**.

The patch-based representation [8], [9] is a more distinctive

¹Photometric error is a main supervisory signal in unsupervised learning.

²Cost volume is constructed to leverage inputs from multiple views.

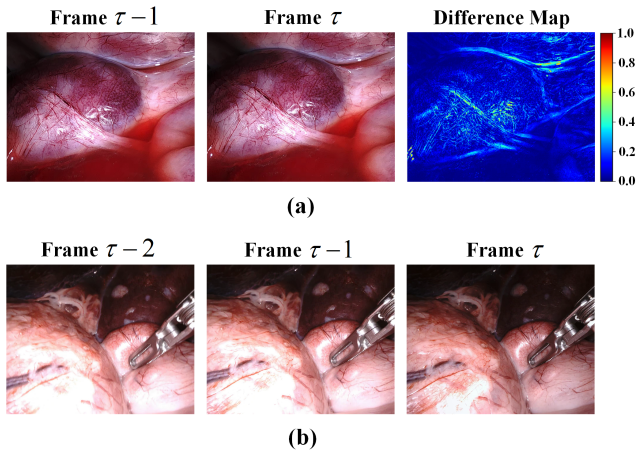


Fig. 2. The main challenges encountered by an unsupervised multi-frame monocular depth estimation model in endoscopic scenes. (a) Low and homogeneous textures. The difference map is acquired by taking an absolute difference between frames τ and $\tau - 1$, to indicate the low-texture and homogeneous-texture regions. (b) Inter-frame brightness fluctuations.

characterization than the point-based representation commonly used in photometric loss. The methods represent a pixel point with a local patch and assume that the pixels within the patch have the same depth. The patch pattern is static, and a 3×3 grid is adopted in [9], for example. We consider the static set of neighbors in previous methods to be problematic, particularly at boundaries and sharp edge areas due to the abrupt changes in depth. Differently, we propose to perform the propagation in an adaptive manner. Our adaptive propagation scheme samples pixels using an offset field generator based on the pixel-wise correlation, which tends to aggregate pixels at the same depth, thus avoiding potential catastrophic errors.

The cross-teaching paradigm aims to strengthen the supervisory signal in regions of brightness fluctuations. We make the observation that AF-SfMLearner [7] accounts for variations in brightness patterns by introducing appearance flow, achieving far less severe errors in the depths of these regions. Intuitively, we leverage the AF-SfMLearner to help teach our model the right answer in brightness fluctuation regions during training, and name this paradigm cross-teaching.

The self-teaching paradigm functions to assist our model in ignoring the detrimental parts in the cost volume and emphasizing instead on the valuable elements. Specifically, we design an appearance simulator to model the edge cases between two frames, *e.g.*, brightness fluctuations and occlusions. We use the frames processed by the appearance simulator and the original frames, respectively, to build cost volumes and enforce the two generated depth maps to be consistent with each other, which we name self-teaching.

To summarize, the main contributions are threefold:

- We propose a novel unsupervised multi-frame depth estimation model for endoscopic scenes, which effectively exploits the temporal information contained in monocular videos in both training and evaluation phases.
- We introduce a learnable patchmatch module for a robust matching in the areas of low and homogeneous textures, which adaptively gathers neighborhood pixels in light of

the pixel-wise correlation.

- We develop cross-teaching and self-teaching paradigms, which provide efficacious regularizations towards brightness fluctuations.

Our SMUDLP exceeds prior state-of-the-art approaches by a large margin on SCARED dataset [10] and Hamlyn dataset³.

II. RELATED WORK

A. Monocular depth estimation

Monocular depth estimation attempts to predict per-pixel depth from a single input image. Supervised methods typically make use of depth supervision from specialist hardware [11] or synthetic data [12]–[14]. As a promising alternative, unsupervised approaches are trained with photometric loss using monocular videos [15] or stereo pairs [16], which eliminates the need for expensive ground-truth depth supervision.

Recently, significant progress has been made in unsupervised monocular endoscopic depth estimation. Turan *et al.* [4] introduced one of the first studies where they applied SfM-Learner [15] to ex-vivo porcine stomach videos. After that, Liu *et al.* [5] proposed the use of sparse depths and camera poses from traditional structure-from-motion (SfM) pipelines to establish a supervisory signal. Ozyoruk *et al.* [1] developed an affine brightness transformer to align the inter-frame brightness condition, and a spatial attention module to encourage the network to emphasize on highly textured regions. Shao *et al.* [17] introduced appearance flow to take into variations in brightness patterns. In addition, they adopted a feature scaling module to mitigate the inadequate representation learning issue induced by low and homogeneous textures. Nevertheless, the attention-based manners as have been done for [1] and [17] do not fundamentally resolve the problem of poor discriminative ability of photometric error in low-texture and homogeneous-texture regions, but rather refines the feature representation on the basis of feature statistics, hence the performance gain is limited. Later in [7], Shao *et al.* generalized the brightness constancy assumption to a dynamic image constraint, allowing for a comprehensive information representation from frame to frame, and designed an automatic registration step to enhance the derivation of appearance flow.

In contrast to the aforementioned methods, our work focuses on exploiting the sequences in the form of video frames during both training and evaluating phases.

B. Multi-frame monocular depth estimation

A growing body of studies extend prior monocular models so that the models can leverage temporal information of video streams to improve the quality of depth estimates at inference time.

Wang *et al.* [18], Zhang *et al.* [19] and Patil *et al.* [20] suggested an idea of combining conventional monocular systems with recurrent networks to process sequences of frames. Similarly, several methods adopted pairs of sequential frames. Wang *et al.* shared features between depth and pose networks. Li *et al.* [6] utilized the current frame together with the depth

³<http://hamlyn.doc.ic.ac.uk/vision/>

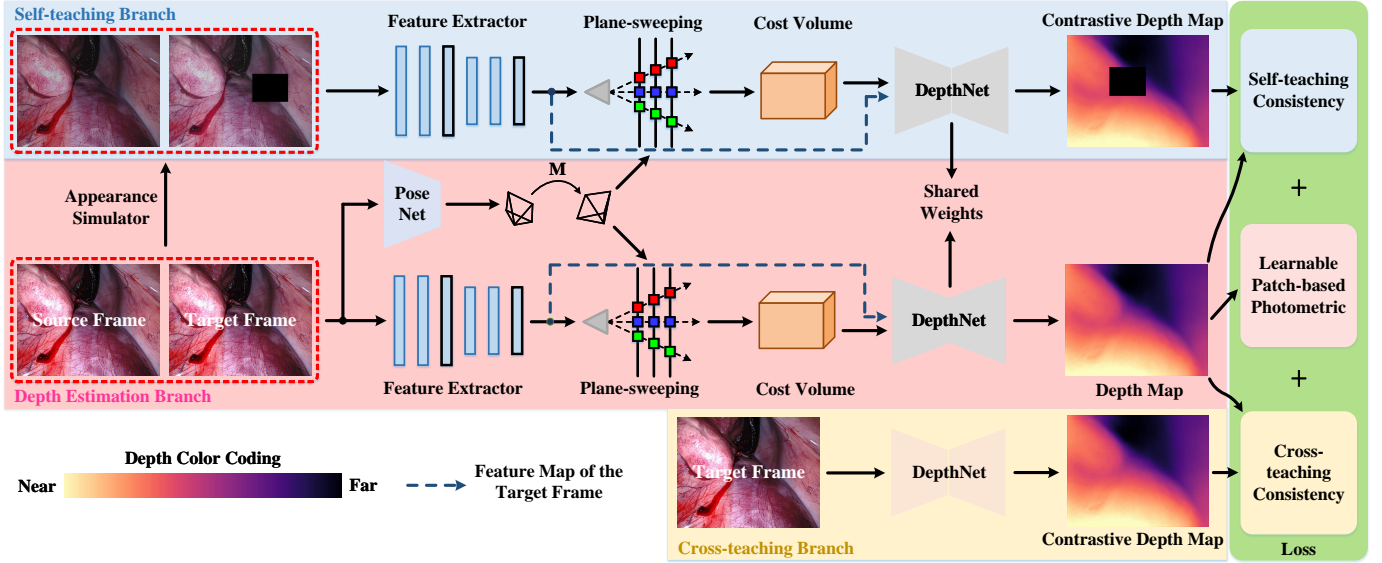


Fig. 3. Overview of the proposed SMUDLP framework. In the training phase, our framework includes a self-teaching branch, a depth estimation branch and a cross-teaching branch. During the evaluation phase, we only apply the depth estimation branch to produce final results.

map from the previous frame as the input of depth network. These methods depend heavily on the temporal representations extracted by the network and do not explicitly reason about the inherent geometry.

Liu *et al.* [21] and Wimbauer *et al.* [22] intergated a plane-sweep stereo cost volume to predict depth map from multiple frames, which shows significant efficacy in improving results. Unfortunately, they require ground-truth depth supervision to circumvent the scale ambiguity of monocular system on the construction of cost volume. Most recently, Watson *et al.* [23] introduced an adaptive cost volume that allows its extents to be learned from data, removing the necessity for ground-truth depth.

In this work, we go one step further and develop an efficacious unsupervised multi-frame monocular depth estimation system for endoscopic scenes, which takes into consideration the unique characteristics of minimally invasive surgery environments, for instance, low and homogeneous textures and inter-frame brightness fluctuations.

III. METHODOLOGY

In this section, we first demonstrate preliminary knowledges of the unsupervised depth estimation. Next, we make use of the plane-sweep stereo to construct a multi-view cost volume. Then, we propose three key innovations that allow a multi-frame monocular depth estimation model to display its real strengths in endoscopic scenes including learnable patchmatch module, cross-teaching and self-teaching paradigms. Finally, we introduce the overall architecture and loss.

A. Preliminaries

The core idea of depth unsupervised learning draws on the warping-based view synthesis, and the framework contains two subnetworks: a depth network (DepthNet) and a pose network (PoseNet). Once the depth of each pixel has been predicted,

the pixel points can be back-projected to a 3D camera space using the camera intrinsic. Then with the predicted relative pose, the generated point cloud can be transformed to another view. Given target frame $I^t(\mathbf{p})$ and source frame $I^s(\mathbf{p})$, the view synthesis is formulated as

$$\mathbf{p}^{s \rightarrow t} = \mathbf{K} \mathbf{M}^{t \rightarrow s} \mathbf{D}^t(\mathbf{p}) \mathbf{K}^{-1} \mathbf{p}^t, \quad (1)$$

where $\mathbf{p}^{s \rightarrow t}$ is the projected pixel coordinates from the target view t to the source view s , \mathbf{p}^t denotes the pixel coordinates in t , \mathbf{K} denotes the camera intrinsic, $\mathbf{M}^{t \rightarrow s}$ denotes the relative pose from t to s , and $\mathbf{D}^t(\mathbf{p})$ stands for the depth map of the target frame $I^t(\mathbf{p})$. We then can acquire a synthesized frame

$$I^{s \rightarrow t}(\mathbf{p}) = I^s \langle \mathbf{p}^{s \rightarrow t} \rangle, \quad (2)$$

where $\langle \cdot \rangle$ denotes the warping operation [24]. The appearance difference of $I^t(\mathbf{p})$ and $I^{s \rightarrow t}(\mathbf{p})$ is delivered as a supervisory signal for the entire training pipeline.

The standard practice [16] to quantify appearance difference is to adopt a weighted L1 loss and structural similarity (SSIM) term [25], referred to as photometric loss

$$\Phi(I^t(\mathbf{p}), I^{s \rightarrow t}(\mathbf{p})) = \alpha \mathcal{L}_{\text{SSIM}} + (1 - \alpha) \mathcal{L}_{\text{L1}}, \quad (3)$$

with

$$\mathcal{L}_{\text{SSIM}} = \frac{1 - \text{SSIM}(I^t(\mathbf{p}), I^{s \rightarrow t}(\mathbf{p}))}{2} \quad (4)$$

and

$$\mathcal{L}_{\text{L1}} = \|I^t(\mathbf{p}) - I^{s \rightarrow t}(\mathbf{p})\|_1, \quad (5)$$

where α is the weight coefficient and is set to 0.85.

B. Plane-sweep stereo cost volume

To leverage sequences of frames, we build a plane-sweep stereo cost volume [26] upon the target camera frustum, which assesses the geometric coherence of pixels from $I^t(\mathbf{p})$ and source frames at different depth values. For the first time we

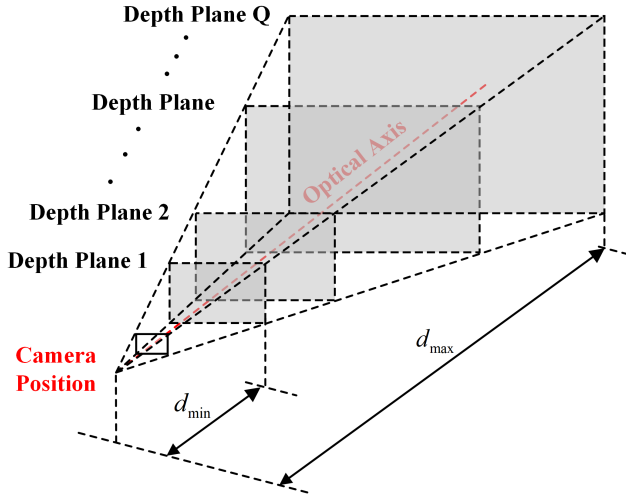


Fig. 4. 3D Illustration of the depth planes in plane-sweeping, with each plane perpendicular to the optical axis.

specify a group of fronto-parallel depth planes linearly spaced between the depth values d_{\min} and d_{\max} , as shown in Fig. 4. Then, for each source frame, we extract a deep feature map and project it to the target camera space using each of the candidate depths, camera intrinsic and predicted relative pose from PoseNet. The final cost volume is built as the average of L1 distances between the warped feature maps and the feature maps from $I^t(\mathbf{p})$ over all source frames. When not otherwise specified, we use one source frame in the construction of cost volume during training. The cost volume and features of the target frame are concatenated as input to DepthNet for depth regression, following [23], [27]. An overview is demonstrated in Fig. 3.

Cost volume allows the monocular system to exploit multiple input frames. However, it requires hyperparameters d_{\min} and d_{\max} to be known. We are unlikely to achieve this because an unsupervised monocular trained depth estimation model can only derive depth ‘up to scale’. To relax this constraint, we make d_{\min} and d_{\max} to be learned from data, following [23]. In each training iteration, the average min and max of depth predictions over a batch are employed to update d_{\min} and d_{\max} using an exponential moving average with a momentum of 0.99. The updated depth range d_{\min} and d_{\max} are saved along with the model weights and remain fixed during the evaluation phase.

C. Learnable patchmatch

To deal with the large low-texture and homogeneous-texture regions in endoscopic scenes, inspired by [8], [9], [28], we propose a **learnable patchmatch module**. Following [9], we select representative keypoints as center pixels in patchmatch. After that, we combine each keypoint with a local patch to enhance their discriminative capabilities. Our patch pattern is dynamic, with neighborhood pixels aggregated in light of the pixel-wise correlation. More details are described below.

1) *Keypoints detection*: We adopt the effective and efficient Direct Sparse Odometry (DSO) [8] to extract keypoints \mathbf{p}_k .

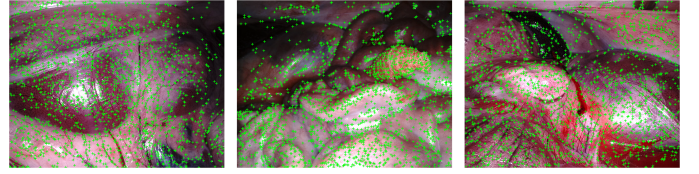


Fig. 5. Illustration of the keypoints, which are extracted by the Direct Sparse Odometry algorithm [8] and marked with green crosses.

See Fig. 5 for an illustration. We augment each keypoint with its local patch, which is referred to as support domain $\Omega_{\mathbf{p}_k}$ and relies on the assumption that pixels within $\Omega_{\mathbf{p}_k}$ are of the same depth.

2) *Adaptive propagation*: Depth spatial coherence inside a local grid is not always satisfied, e.g., at anatomical boundaries and sharp edge regions. Hence, instead of adopting a static set of neighbors, such as a 3×3 grid as done for [9], we propose sampling neighborhood pixels via adaptive propagation. Fig. 6 depicts the functionality of our adaptive scheme, which tends to aggregate pixels from the same surface, avoiding the catastrophic errors induced by using just a fixed pattern.

We base the implementation of our adaptive propagation scheme on Deformable Convolution Networks [28]. To gather $N_{\mathbf{p}_k}$ pixels for each keypoints, we carefully design an offset field generator to learn additional offset fields $\{\Delta \mathbf{o}_i(\mathbf{p}_k)\}_{i=1}^{N_{\mathbf{p}_k}}$ placed on top of a basic 2D offset grid $\{\mathbf{o}_i\}_{i=1}^{N_{\mathbf{p}_k}}$. $N_{\mathbf{p}_k}$ is set to 8 in our experiments, following [9]. As shown in Fig. 7, we first measure the feature similarity of the targeted keypoint \mathbf{p}_k and its surrounding pixels \mathbf{p}_k' to encourage the derivation of additional offset fields. Mathematically,

$$\mathbf{c}(\mathbf{p}_k; \mathbf{r}) = \mathcal{F}(\mathbf{p}_k) \odot \mathcal{F}(\mathbf{p}_k') / \ell, \quad (6)$$

where \mathbf{c} denotes the correlation vector, \mathbf{r} denotes the search range and is empirically set to a 8×8 window in this work, \mathcal{F} denotes the feature map, \odot denotes the dot product, and ℓ denotes the length of feature descriptor. Then, a self-correlation volume is constructed by integrating all correlation vectors into a 3D grid. We finally apply two layers of convolution to decode offset fields from the self-correlation volume. The procedure is similar to flow decoding in optical flow estimation [27]. With the learned additional offset fields, we can obtain our support domain

$$\Omega_{\mathbf{p}_k} = \{\mathbf{p}_k + \mathbf{o}_i + \Delta \mathbf{o}_i(\mathbf{p}_k)\}_{i=1}^{N_{\mathbf{p}_k}} \cup \{\mathbf{p}_k\}, \quad (7)$$

where \cup denotes the union of sets. Moreover, we can acquire the depths of sampled pixels in $\Omega_{\mathbf{p}_k}$ via the warping operation

$$\mathbf{D}(\Omega_{\mathbf{p}_k}) = \{\mathbf{D}(\mathbf{p}_k + \mathbf{o}_i + \Delta \mathbf{o}_i(\mathbf{p}_k))\}_{i=1}^{N_{\mathbf{p}_k}} \cup \{\mathbf{D}(\mathbf{p}_k)\}. \quad (8)$$

3) *Learnable patch-based photometric loss*: Different from traditional view synthesis in unsupervised depth learning, we project each keypoint using depths $\mathbf{D}(\Omega_{\mathbf{p}_k})$ from the support domain. We can thus reformulate Eq. 1 as

$$\Omega_{\mathbf{p}_k}^{s \rightarrow t} = \mathbf{K} \mathbf{M}^{t \rightarrow s} \mathbf{D}^t(\Omega_{\mathbf{p}_k}) \mathbf{K}^{-1} \mathbf{p}_k^t. \quad (9)$$

It should be noted that, our patch-based view synthesis also differs from [9], which uses depth of each keypoint to project

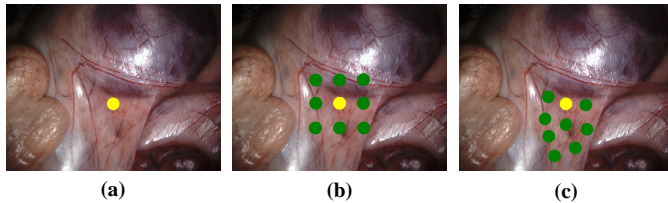


Fig. 6. Illustration of the sampled locations in regular patchmatch and our learnable patchmatch. (a) Target image. (b) Sampled locations of fixed propagation pattern in regular patchmatch. (c) Sampled locations of adaptive propagation pattern in our approach.

the support domain. We do this not only to supervise the depth of keypoints, but also to supervise the depth of non-keypoint regions using a more discriminative supervision signal at each keypoint. Besides, this retains the distinctive characterization in [9]. Substituting $\Omega_{\mathbf{p}_k}^{s \rightarrow t}$ into Eq. 2, we obtain

$$I^{s \rightarrow t}(\Omega_{\mathbf{p}_k}) = I^s \langle \Omega_{\mathbf{p}_k}^{s \rightarrow t} \rangle. \quad (10)$$

According to Eq. 3 and Eq. 10, we can acquire our learnable patch-based photometric loss

$$\mathcal{L}_{ph} = \Phi(I^t(\mathbf{p}_k), I^{s \rightarrow t}(\Omega_{\mathbf{p}_k})), \quad (11)$$

\mathcal{L}_{ph} is accumulated over each support domain, which allows a larger area of valid gradients with a wider convergence basin. In order to alleviate the negative impacts of occluded pixels on \mathcal{L}_{ph} , we use two source frames $I^s(\mathbf{p}) \in \{I^{t-1}(\mathbf{p}), I^{t+1}(\mathbf{p})\}$ in the photometric loss, and follow [29] to choose the one with the minimum \mathcal{L}_{ph} . Note that the source frames used in \mathcal{L}_{ph} are not the same as the source frames to build cost volume.

D. Cross-teaching

To reinforce the supervisory signal in regions of brightness fluctuations, we propose a **cross-teaching paradigm**, inspired by the observation that AF-SfMLearner [7] achieves far less severe mistakes in the depth of these regions as a result of the introduced appearance flow. However, adding the appearance flow term into photometric loss, as done for AF-SfMLearner, leads to expensive memory consumption. We therefore leverage the trained depth network by AF-SfMLearner as a teacher to guide our model towards the correct depth even in areas with large brightness changes, which is more memory efficient. For each training sample, this separate network yields a depth map $\hat{\mathbf{D}}^t(\mathbf{p})$ and is discarded when the training is completed. Mathematically,

$$\mathcal{L}_{ct} = \frac{|\mathbf{D}^t(\mathbf{p}) - \hat{\mathbf{D}}^t(\mathbf{p})|}{\mathbf{D}^t(\mathbf{p}) + \hat{\mathbf{D}}^t(\mathbf{p})}, \quad (12)$$

where \mathcal{L}_{ct} denotes the cross-teaching consistency loss. Gradients flowing to $\hat{\mathbf{D}}^t(\mathbf{p})$ are blocked to guarantee that teacher delivers knowledge to student and not vice versa. Here, instead of using their absolute difference directly, we normalize the absolute difference by their sum. This is more intuitive since points with differing absolute depths are treated equally during optimization. In addition, the outputs are scale-invariant with a natural range of 0 to 1, which is beneficial to the numerical stability throughout training.

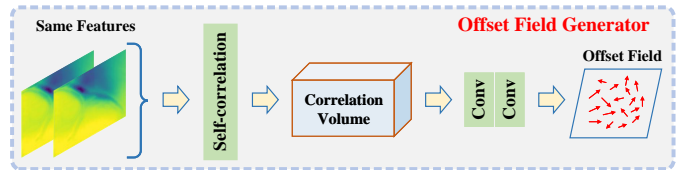


Fig. 7. Offset field generator. We use the penultimate layer feature map of DepthNet to construct the correlation volume for offset field decoding. Note that Conv stands for the 3×3 convolution layer, and the activation behind Conv is the ELU [30].

E. Self-teaching

We develop a **self-teaching paradigm** to assist our model in being immune to the harmful information in the cost volume, such as that induced by brightness fluctuations and occlusions, and focusing on the valuable elements. Towards this end, we design an appearance simulator consisting of random gamma correction, color jitter and masking to simulate the edge cases. We use the frames derived by the appearance simulator and the original frames to build cost volumes, respectively, and enforce the two resulting depth maps to be consistent with each other, which provides robustness against brightness fluctuations and occlusions. The self-teaching consistency loss is defined as

$$\mathcal{L}_{st} = \frac{|\mathbf{D}^t(\mathbf{p}) - \bar{\mathbf{D}}^t(\mathbf{p})|}{\mathbf{D}^t(\mathbf{p}) + \bar{\mathbf{D}}^t(\mathbf{p})} * \mathbf{R}(\mathbf{p}), \quad (13)$$

where $\bar{\mathbf{D}}^t(\mathbf{p})$ represents the depth map of transformed frames, $*$ denotes the element-wise multiplication, and $\mathbf{R}(\mathbf{p})$ denotes the unoccluded mask, determined by random masking. Gradients to $\mathbf{D}^t(\mathbf{p})$ are blocked. We will describe the components of the appearance simulator in detail below including random gamma correction, color jitter and masking.

Gamma correction is a non-linear mapping used to adjust the illuminance of images. During the data acquisition process of the endoscopic scenes, there are severe brightness fluctuations caused by illumination variations. To simulate the varied illuminations, we incorporate random gamma correction.

Color Jitter mainly involves lightness, saturation, hue and contrast jitters. We integrate random color jitter to simulate the complicated non-Lambertian reflections and inter-reflections in minimally invasive surgery environments.

Masking is intended to mimic the occlusions among multiple input frames. Specifically, we generate a binary mask to randomly crop some portions on target frame, and then adopt the inverted binary mask as a ground-truth of the mimicked occlusion in self-teaching consistency loss, which contributes to make the model insensitive to occlusion, that is, even when there is occlusion, the model can still correctly predict the depth of the unoccluded areas.

F. Overall architecture and loss

Fig. 3 presents an overview of the overall framework, which involves three parts: depth estimation branch, cross-teaching branch and self-teaching branch. Our feature extractor, DepthNet and PoseNet share similar structures to [23]. Apart from the learnable patch-based photometric loss \mathcal{L}_{ph} , cross-teaching

consistency loss \mathcal{L}_{ct} and self-teaching consistency loss \mathcal{L}_{st} , we make use of an edge-aware smoothness loss to encourage the smoothness property of depth map

$$\mathcal{L}_{es} = |\nabla \mathbf{D}(\mathbf{p})| * e^{-\nabla |I^t(\mathbf{p})|}, \quad (14)$$

which is proposed in [16].

The total optimization objective is defined as follows

$$\mathcal{L} = \lambda_1 \mathcal{L}_{ph} + \lambda_2 \mathcal{L}_{ct} + \lambda_3 \mathcal{L}_{st} + \lambda_4 \mathcal{L}_{es}, \quad (15)$$

where the weights are empirically set as: $\lambda_1 = 1$, $\lambda_2 = 0.02$, $\lambda_3 = 0.002$, $\lambda_4 = 0.0001$.

IV. EXPERIMENT

To verify the efficacy of our SMUDLP, we provide comparisons of depth and point cloud, and intensive ablation studies on the SCARED dataset. We follow the split established by [7], which consists of 15351, 1705 and 551 images for the training, validation and test sets, respectively. In addition, we present a generalization study on the Hamlyn dataset [31].

A. Datasets

- **SCARED** [10] involves 35 endoscopic videos collected from porcine cadaver abdominal anatomy, along with the point cloud and ego-motion ground truths.
- **Hamlyn**⁴ consists of real endoscopic videos and phantom heart model videos. We adopt the dataset processed by Recasens *et al.* [31], where they annotate the real videos with ground-truth depth using the Efficient Large-Sacle Stereo Matching algorithm [32].

B. Experimental Settings

1) *Training*: The proposed SMUDLP is implemented in the PyTorch library [33]. We train with the Adam optimizer [34], where $\beta_1 = 0.9$, $\beta_2 = 0.99$ and a batch size of 12. The total number of epochs is set to 20 and the initial learning rate is 10^{-4} , dropping by a factor of 10 after 10 epochs. The input resolution is 320×256 pixels. As with existing works [1], [7], [23], we use weights pretrained on ImageNet [35]. We perform static cameras and start of sequences augmentations the same as [23]. Under these settings, the SMUDLP converges on a single NVIDIA Titan RTX in about seven hours.

2) *Performance metrics*: We adopt the standard evaluation metrics as in previous studies [7], [23]:

- Abs Rel: $\frac{1}{|\mathbf{D}|} \sum_{d \in \mathbf{D}} |d^* - d|/d^*$;
- Sq Rel: $\frac{1}{|\mathbf{D}|} \sum_{d \in \mathbf{D}} |d^* - d|^2/d^*$;
- RMSE: $\sqrt{\frac{1}{|\mathbf{D}|} \sum_{d \in \mathbf{D}} |d^* - d|^2}$;
- RMSE log: $\sqrt{\frac{1}{|\mathbf{D}|} \sum_{d \in \mathbf{D}} |\log d^* - \log d|^2}$;
- δ : $\frac{1}{|\mathbf{D}|} \left\{ \left| d \in \mathbf{D} \mid \max \left(\frac{d^*}{d}, \frac{d}{d^*} < 1.25 \right) \right\} \times 100\%$

Since the monocular depth estimation system suffers from scale ambiguity, we apply a median scaling technique [15] to

the predicted depth maps for evaluation, which can be written as

$$\mathbf{D}_{scaled} = (\mathbf{D}_{pred} * (\text{median}(\mathbf{D}_{gt}) / \text{median}(\mathbf{D}_{pred}))). \quad (16)$$

Following [7], we clip the scaled depth maps at 150 mm on the SCARED and Hamlyn datasets.

C. Comparison to state-of-the-art competitors

We compare our SMUDLP against prior state-of-the-arts on depth estimation and point cloud estimation.

1) *Depth estimation*: Table I demonstrates the depth comparison results on the SCARED dataset, including monocular methods SfMLearner [15], DeFeat-Net [36], Monodepth2 [29], Endo-SfM [1], AF-SfMLearner [7] and multi-frame monocular method ManyDepth [23]. The results of monocular method are inherited from [7]. We reproduce ManyDepth with the official implementation⁵. As can be seen, our SMUDLP outperforms the compared methods by a significant margin. In particular, our approach improves AF-SfMLearner by more than 10% and ManyDepth by more than 15% on most metrics. Besides, the results of multi-frame monocular methods are generally better than those of monocular methods, which reveals that additional frames are valuable and contribute to the accuracy gains. It is worth noting that while SMUDLP and ManyDepth both use only two frames to construct the cost volume during the training phase, when more frames are put into the cost volume building at inference time, SMUDLP can always improve the accuracy, whereas ManyDepth fails. Fig. 12 presents the qualitative comparisons, showing that the depth maps predicted by SMUDLP avoid catastrophic failures and display finer details of tissue structure, such as anatomical boundaries.

In Fig. 8 (a), we present the results on RMSE at different clipped depth values, and the SMUDLP is capable of achieving superior results at different range distances. Interestingly, the multi-frame monocular depth estimation methods ManyDepth and SMUDLP improve largely at close distances, but this improvement gradually decreases with the increasing distances. The reason behind this phenomenon may be that the disparities between two frames are larger at close distances, therefore the additional frames can provide more complementary information. However, the disparities at distant distances are almost zero, which means that the distant contents in two frames are nearly identical, so it is equivalent to using the information of only one image.

2) *Point cloud estimation*: We generate point clouds using the depth predictions and camera intrinsic. To overcome the inherent scale ambiguity, we adopt the same median scaling strategy as in depth evaluation. Table II summarizes the point cloud comparison results on the SCARED dataset, indicating that our SMUDLP outperforms the compared methods, both monocular and multi-frame monocular.

We believe the inferior performance of these methods lies in weakened supervisory signal and lacking of ability to exploit temporal information. SfMLearner, DeFeat-Net, Monodepth2 and ManyDepth are heavily affected by the unique inter-frame

⁴<http://hamlyn.doc.ic.ac.uk/vision/>

⁵<https://github.com/nianticlabs/manydepth>

TABLE I

QUANTITATIVE DEPTH COMPARISON ON THE SCARED DATASET. V DENOTES THE INPUT VIEWS. CIs DENOTES THE CONFIDENCE INTERVALS. ON ALL METRICS, THE PAIRED P-VALUES OF OURS AND THE COMPARED METHODS ARE LESS THAN 0.05. THE TOP TWO RESULTS ARE HIGHLIGHTED IN RED AND BLUE.

Method	V	Abs Rel ↓	95% CIs	Sq Rel ↓	95% CIs	RMSE ↓	95% CIs	RMSE log ↓	95% CIs	$\delta \uparrow$	95% CIs
SfMLearner [15]	1	0.079	[0.076, 0.081]	0.879	[0.794, 0.964]	6.896	[6.513, 7.279]	0.110	[0.106, 0.115]	0.947	[0.942, 0.952]
DeFeat-Net [36]	1	0.077	[0.074, 0.079]	0.792	[0.731, 0.853]	6.688	[6.355, 7.021]	0.108	[0.104, 0.112]	0.941	[0.936, 0.946]
Monodepth2 [29]	1	0.071	[0.068, 0.073]	0.590	[0.554, 0.627]	5.606	[5.404, 5.809]	0.094	[0.091, 0.097]	0.953	[0.948, 0.957]
Endo-SfM [1]	1	0.062	[0.060, 0.065]	0.606	[0.551, 0.661]	5.726	[5.396, 6.056]	0.093	[0.089, 0.097]	0.957	[0.952, 0.961]
AF-SfMLearner [7]	1	0.059	[0.057, 0.061]	0.435	[0.406, 0.464]	4.925	[4.729, 5.122]	0.082	[0.079, 0.084]	0.974	[0.971, 0.977]
ManyDepth [23]	2	0.061	[0.059, 0.063]	0.505	[0.466, 0.543]	5.371	[5.112, 5.631]	0.087	[0.084, 0.090]	0.967	[0.964, 0.971]
SMUDLP (ours)	2	0.051	[0.050, 0.053]	0.386	[0.354, 0.417]	4.675	[4.451, 4.899]	0.074	[0.072, 0.077]	0.979	[0.977, 0.982]
ManyDepth [23]	3	0.062	[0.060, 0.064]	0.511	[0.473, 0.549]	5.415	[5.160, 5.669]	0.088	[0.085, 0.091]	0.966	[0.963, 0.970]
SMUDLP (ours)	3	0.051	[0.049, 0.052]	0.374	[0.344, 0.405]	4.615	[4.393, 4.838]	0.073	[0.071, 0.076]	0.980	[0.977, 0.982]
ManyDepth [23]	4	0.064	[0.062, 0.066]	0.527	[0.489, 0.565]	5.494	[5.243, 5.745]	0.090	[0.087, 0.094]	0.964	[0.960, 0.968]
SMUDLP (ours)	4	0.051	[0.049, 0.052]	0.370	[0.340, 0.400]	4.600	[4.380, 4.820]	0.073	[0.071, 0.076]	0.980	[0.977, 0.983]
ManyDepth [23]	5	0.066	[0.064, 0.068]	0.544	[0.506, 0.583]	5.572	[5.323, 5.821]	0.092	[0.089, 0.096]	0.961	[0.957, 0.965]
SMUDLP (ours)	5	0.051	[0.049, 0.053]	0.368	[0.338, 0.397]	4.597	[4.380, 4.814]	0.073	[0.071, 0.076]	0.980	[0.977, 0.983]

TABLE II

POINT CLOUD COMPARISON ON THE SCARED DATASET. ON ALL METRICS, THE PAIRED P-VALUES OF OURS AND THE COMPARED METHODS ARE LESS THAN 0.05.

Method	V	Abs Rel ↓	95% CIs	Sq Rel ↓	95% CIs	RMSE ↓	95% CIs	RMSE log ↓	95% CIs	MSE ↓	95% CIs
SfMLearner [15]	1	0.087	[0.084, 0.091]	0.480	[0.431, 0.528]	4.446	[4.192, 4.701]	0.120	[0.116, 0.124]	29.021	[25.424, 32.617]
DeFeat-Net [36]	1	0.085	[0.081, 0.089]	0.424	[0.390, 0.457]	4.302	[4.083, 4.520]	0.118	[0.114, 0.122]	25.345	[22.597, 28.092]
Monodepth2 [29]	1	0.079	[0.076, 0.083]	0.319	[0.299, 0.338]	3.614	[3.482, 3.747]	0.105	[0.102, 0.108]	15.567	[14.459, 16.675]
Endo-SfM [1]	1	0.071	[0.067, 0.074]	0.331	[0.299, 0.362]	3.702	[3.483, 3.920]	0.105	[0.101, 0.108]	20.521	[17.846, 23.195]
AF-SfMLearner [7]	1	0.068	[0.065, 0.071]	0.234	[0.218, 0.249]	3.174	[3.046, 3.302]	0.094	[0.091, 0.096]	12.429	[11.364, 13.495]
ManyDepth [23]	2	0.070	[0.067, 0.073]	0.276	[0.254, 0.297]	3.476	[3.303, 3.648]	0.099	[0.096, 0.102]	16.341	[14.512, 18.171]
SMUDLP (ours)	2	0.060	[0.057, 0.063]	0.209	[0.192, 0.226]	3.020	[2.873, 3.167]	0.087	[0.085, 0.090]	12.216	[10.873, 13.560]
ManyDepth [23]	3	0.071	[0.068, 0.074]	0.279	[0.258, 0.300]	3.503	[3.334, 3.672]	0.100	[0.097, 0.103]	16.363	[14.571, 18.154]
SMUDLP (ours)	3	0.059	[0.056, 0.062]	0.203	[0.186, 0.220]	2.982	[2.835, 3.128]	0.087	[0.084, 0.089]	11.959	[10.629, 13.288]
ManyDepth [23]	4	0.073	[0.069, 0.076]	0.287	[0.266, 0.308]	3.552	[3.385, 3.719]	0.102	[0.099, 0.104]	16.594	[14.832, 18.357]
SMUDLP (ours)	4	0.059	[0.056, 0.062]	0.200	[0.184, 0.217]	2.971	[2.827, 3.116]	0.086	[0.084, 0.089]	11.821	[10.519, 13.124]
ManyDepth [23]	5	0.075	[0.071, 0.078]	0.296	[0.275, 0.317]	3.600	[3.435, 3.766]	0.103	[0.100, 0.106]	16.881	[15.131, 18.631]
SMUDLP (ours)	5	0.060	[0.057, 0.063]	0.199	[0.183, 0.215]	2.969	[2.826, 3.112]	0.086	[0.084, 0.089]	11.728	[10.457, 13.000]

TABLE III

QUANTITATIVE DEPTH COMPARISON ON THE HAMLYN DATASET. ALL MODELS ARE UNSUPERVISED TRAINED ON THE SCARED DATASET. ON ALL METRICS, THE PAIRED P-VALUES OF OURS AND THE COMPARED METHODS ARE LESS THAN 0.05.

Method	V	Abs Rel ↓	95% CIs	Sq Rel ↓	95% CIs	RMSE ↓	95% CIs	RMSE log ↓	95% CIs	$\delta \uparrow$	95% CIs
SfMLearner [15]	1	0.152	[0.142, 0.162]	2.582	[2.151, 3.012]	10.481	[9.418, 11.544]	0.205	[0.194, 0.217]	0.761	[0.737, 0.785]
DeFeat-Net [36]	1	0.143	[0.132, 0.154]	2.663	[2.136, 3.191]	10.323	[9.155, 11.491]	0.191	[0.179, 0.204]	0.797	[0.772, 0.822]
Monodepth2 [29]	1	0.167	[0.155, 0.179]	3.383	[2.728, 4.037]	11.239	[10.000, 12.477]	0.205	[0.193, 0.218]	0.758	[0.732, 0.783]
Endo-SfM [1]	1	0.147	[0.135, 0.158]	2.800	[2.234, 3.366]	10.207	[9.025, 11.390]	0.188	[0.175, 0.200]	0.795	[0.768, 0.821]
AF-SfMLearner [7]	1	0.143	[0.132, 0.154]	2.561	[2.066, 3.055]	10.065	[8.971, 11.160]	0.188	[0.177, 0.200]	0.796	[0.772, 0.821]
ManyDepth [23]	2	0.155	[0.145, 0.165]	2.743	[2.228, 3.257]	10.367	[9.209, 11.524]	0.194	[0.182, 0.206]	0.781	[0.756, 0.806]
SMUDLP (ours)	2	0.138	[0.128, 0.148]	2.316	[1.840, 2.792]	9.351	[8.286, 10.416]	0.175	[0.164, 0.186]	0.810	[0.785, 0.836]

brightness fluctuations and low and homogeneous textures of endoscopic scenes. While Endo-SfM and AF-SfMLearner are specifically designed for endoscopic scenarios, they cannot enhance their depth estimates by leveraging valuable additional frames. In contrast, our SMUDLP could benefit from both.

D. Generalization on the Hamlyn dataset

We study the model generalization ability to validate that our SMUDLP indeed learns transferable features, not simply memorizing training samples. To this end, we apply the models trained on SCARED to the Hamlyn dataset for evaluation with-

out any fine-tuning. The test frames are resized to 320×256 pixels. As presented in Table III, the superior results indicate that our SMUDLP generalizes well across different patients and cameras. Fig. 8 (b) shows the generalization performance on RMSE at different clipped depth values.

E. Ablation studies

To figure out the impact of each component on performance, we conduct multiple ablation studies at a more granular level, including SMUDLP, number of input views and break-down comparison of learnable patchmatch module.

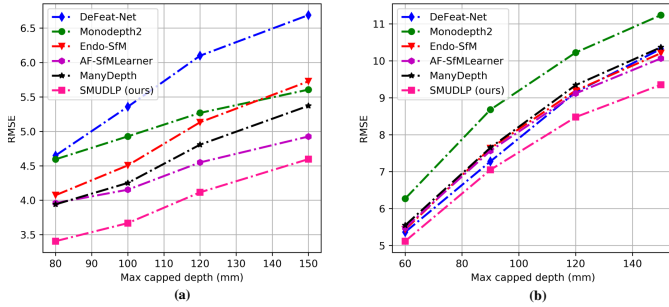


Fig. 8. The RMSE results at different clipped depth ranges. (a) SCARED dataset. (b) Hamlyn dataset. The results of ManyDepth and SMUDLP are reported with an input view of 2.

TABLE IV
ABLATION STUDY ON THE SMUDLP. CV: COST VOLUME; LPM:
LEARNABLE PATCHMATCH MODULE; CT: CROSS-TEACHING; ST:
SELF-TEACHING.

ID	CV	LPM	CT	ST	Abs Rel ↓	Sq Rel ↓	RMSE ↓	RMSE log ↓
1					0.072	0.635	6.047	0.099
2	✓				0.068	0.560	5.494	0.092
3	✓	✓			0.059	0.443	4.996	0.082
4	✓	✓	✓		0.055	0.410	4.825	0.078
5	✓	✓	✓	✓	0.051	0.386	4.675	0.074

TABLE V
BREAK-DOWN COMPARISON OF LEARNABLE PATCHMATCH MODULE.
SAM: SPATIAL ATTENTION MODULE [1]; FSM: FEATURE SCALING
MODULE [17]; PM [9]: PATCHMATCH MODULE; LPM: LEARNABLE
PATCHMATCH MODULE.

ID	SAM	FSM	PM	LPM	Abs Rel ↓	Sq Rel ↓	RMSE ↓	RMSE log ↓
1					0.072	0.635	6.047	0.099
2	✓				0.070	0.582	5.818	0.095
3		✓			0.069	0.562	5.620	0.093
4			✓		0.066	0.532	5.414	0.092
5				✓	0.063	0.487	5.183	0.086

1) *SMUDLP (Table IV)*: We start with the underperforming baseline (ID 1). By first adding the cost volume, we observe a slight improvement in performance (ID 2). However, the accuracy is still far from satisfactory yet. ID 3 presents an addition of the learnable patch module, which adaptively increases the discriminative ability in low-texture and homogeneous-texture regions and displays considerable efficacy in boosting performance. We then add the cross-teaching paradigm to strengthen the supervisory signal in the regions of brightness fluctuations, again with a consistent improvement in all evaluation metrics (ID 4). We finally incorporate the self-teaching paradigm and forms our SMUDLP, which achieves the best results (ID 5).

2) *Number of input views (Fig. 9)*: We evaluate the performance under input views 2, 3, and 4 during the training and evaluation phases, respectively. Note that the models of Ours (test), Ours w/o ST (test) and ManyDepth have an input view of 2 during training. It can be seen that when increasing the input views in the training phase, the accuracy gains are small, which is consistent with the finding in ManyDepth. However, unlike ManyDepth, SMUDLP always improves accuracy when

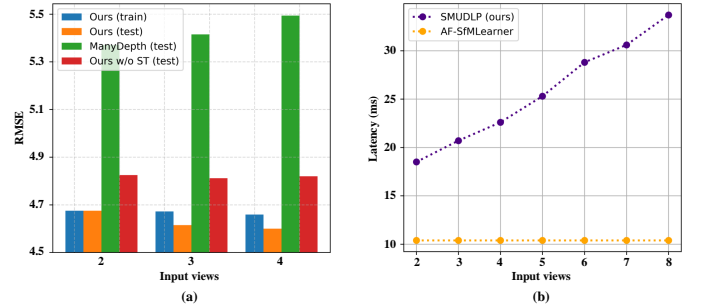


Fig. 9. Ablation study on the number of input views. (a) Accuracy. (b) Latency.

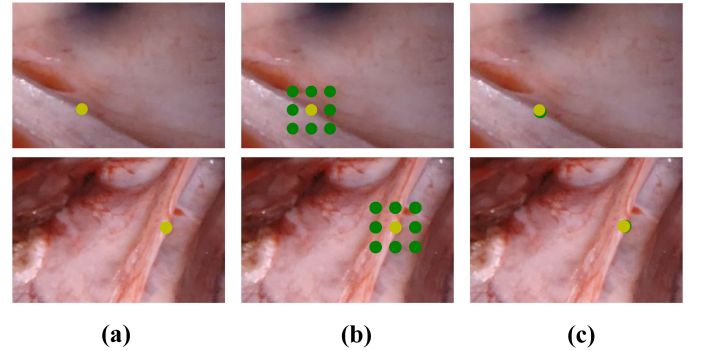


Fig. 10. Visualization of the sampled locations in sharp edge regions. (a) Target image. (b) Sampled locations in patchmatch module [9]. (c) Sampled locations in our learnable patchmatch module.

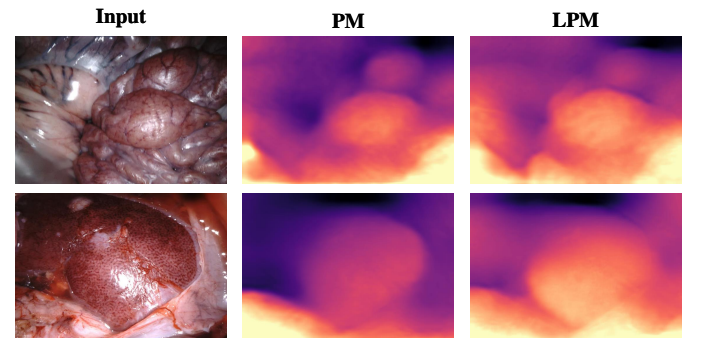


Fig. 11. Qualitative depth results for ID 4 (patchmatch module [9]) and ID 5 (learnable patchmatch module) in Table V.

appending input views at inference time. To dig out why, we further show the depth accuracy after ablating the self-teaching paradigm and find that it roughly matches the case of ManyDepth, revealing that the self-teaching paradigm allows model to leverage more frames to enhance the depth estimate at inference time, although only two frames are used during training. This is not surprising given that the self-teaching paradigm can teach model to ignore the detrimental information and focus on the meaningful elements. As the number of frames increases, so do the occlusions and brightness variations between source and target frames, which are disasters for other approaches but not for our SMUDLP equipped with self-teaching. In addition, we present the latency of SMUDLP under different input views and report the latency of AF-SfMLearner as a baseline. While

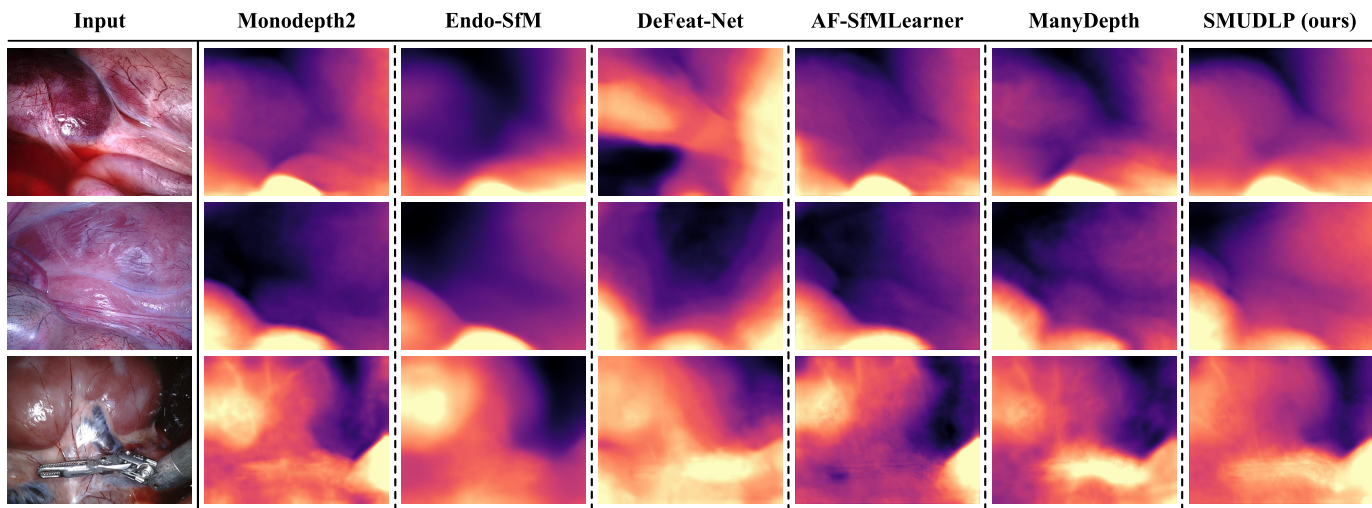


Fig. 12. Qualitative depth comparison of our method against the compared methods on the SCARED dataset. Our method delivers more continuous depth maps with finer-grained details, *e.g.*, anatomical boundaries.

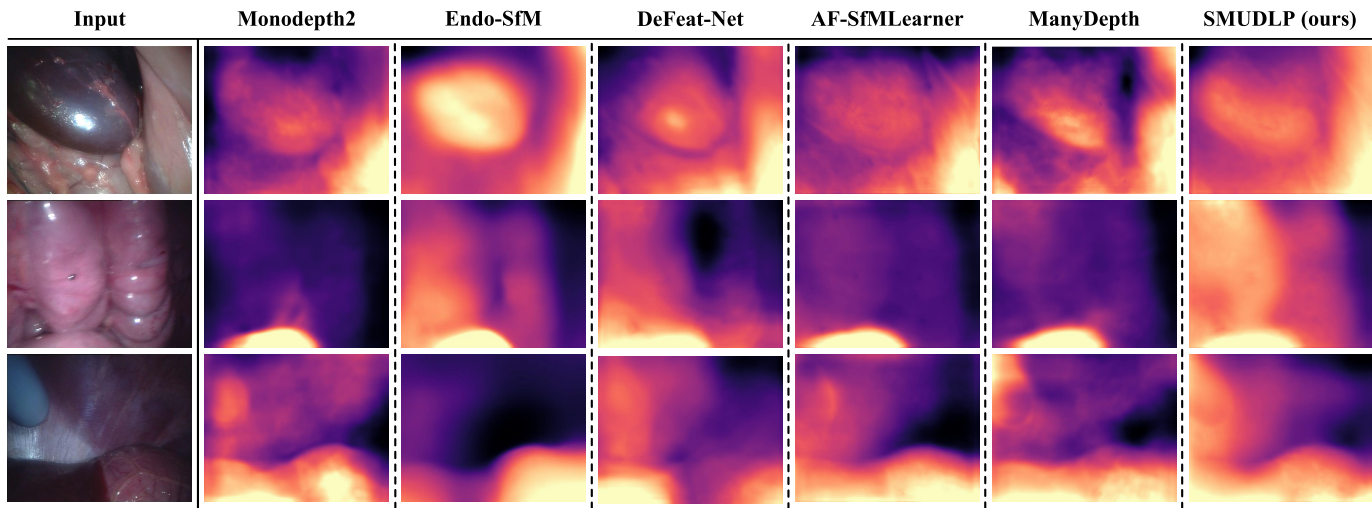


Fig. 13. Qualitative depth comparison on the Hamlyn dataset.

the latency increases with input views, our SMUDLP can still meet real-time requirements.

3) *Break-down comparison of learnable patchmatch module (Table V)*: To further present the superiority of learnable patchmatch module, we perform comparisons with other alternative methods, including spatial attention module [1], patchmatch module [9], and feature scaling module [7]. It can be seen that our adaptive patchmatch module outperforms other alternative methods by a large margin. Fig. 10 shows the sampled locations of patchmatch module and learnable patchmatch module in the sharp edge regions. Our learnable patchmatch module avoids severe errors by adaptively aggregating pixels near the center point. Fig. 11 shows the qualitative depth comparisons of patchmatch module and learnable patchmatch module. The depth maps of our learnable patchmatch module preserve sharp edges and boundaries.

V. CONCLUSION

In this work, we present a novel unsupervised framework SMUDLP, which predicts superior depths from multiple endoscopic frames. On the one hand, the SMUDLP can integrate a learnable patchmatch module to increase the discriminative capability in low-texture and homogeneous-texture regions. On the other hand, the SMUDLP can enforce cross-teaching and self-teaching consistencies to provide efficacious regularizations towards brightness variations. When more frames are put into the cost volume building during the evaluation phase, the SMUDLP can always improve the depth accuracy, even though only two frames are leveraged during training. This enables us to adjust the number of input views in light of the requirements for accuracy. We are confident that the introduced innovations can be applied to more general scenarios, for instance, indoor environments. Extensive experiments on both the SCARED and Hamlyn datasets indicate the efficacy of SMUDLP.

REFERENCES

- [1] K. B. Ozyoruk, G. I. Gokceler, T. L. Bobrow, G. Coskun, K. Inctan, Y. Almalioglu, F. Mahmood, E. Curto, L. Perdigoto, M. Oliveira, *et al.*, "Endoslam dataset and an unsupervised monocular visual odometry and depth estimation approach for endoscopic videos: Endo-sfmlearner," *Medical Image Analysis*, 2021.
- [2] A. Sinha, X. Liu, A. Reiter, M. Ishii, G. D. Hager, and R. H. Taylor, "Endoscopic navigation in the absence of ct imaging," in *International Conference on Medical Image Computing and Computer-Assisted Intervention*, pp. 64–71, Springer, 2018.
- [3] L. Chen, W. Tang, N. W. John, T. R. Wan, and J. J. Zhang, "Slam-based dense surface reconstruction in monocular minimally invasive surgery and its application to augmented reality," *Computer Methods and Programs in Biomedicine*, vol. 158, pp. 135–146, 2018.
- [4] M. Turan, E. P. Ornek, N. Ibrahimli, C. Giracoglu, Y. Almalioglu, M. F. Yanik, and M. Sitti, "Unsupervised odometry and depth learning for endoscopic capsule robots," in *2018 IEEE/RSJ International Conference on Intelligent Robots and Systems*, pp. 1801–1807, IEEE, 2018.
- [5] X. Liu, A. Sinha, M. Ishii, G. D. Hager, A. Reiter, R. H. Taylor, and M. Unberath, "Dense depth estimation in monocular endoscopy with self-supervised learning methods," *IEEE Transactions on Medical Imaging*, vol. 39, no. 5, pp. 1438–1447, 2019.
- [6] L. Li, X. Li, S. Yang, S. Ding, A. Jolfaei, and X. Zheng, "Unsupervised-learning-based continuous depth and motion estimation with monocular endoscopy for virtual reality minimally invasive surgery," *IEEE Transactions on Industrial Informatics*, vol. 17, no. 6, pp. 3920–3928, 2020.
- [7] S. Shao, Z. Pei, W. Chen, W. Zhu, X. Wu, D. Sun, and B. Zhang, "Self-supervised monocular depth and ego-motion estimation in endoscopy: Appearance flow to the rescue," *Medical Image Analysis*, p. 102338, 2022.
- [8] J. Engel, V. Koltun, and D. Cremers, "Direct sparse odometry," *IEEE Transactions on Pattern Analysis and Machine Intelligence*, vol. 40, no. 3, pp. 611–625, 2017.
- [9] Z. Yu, L. Jin, and S. Gao, "P²net: Patch-match and plane-regularization for unsupervised indoor depth estimation," in *Computer Vision—ECCV 2020: 16th European Conference, Glasgow, UK, August 23–28, 2020, Proceedings, Part XXIV 16*, pp. 206–222, Springer, 2020.
- [10] M. Allan, J. Mcleod, C. C. Wang, J. C. Rosenthal, K. X. Fu, T. Zefiro, W. Xia, Z. Zhanshi, H. Luo, and X. Zhang, "Stereo correspondence and reconstruction of endoscopic data challenge," *arXiv preprint arXiv:2101.01133*, 2021.
- [11] D. Eigen, C. Puhrsch, and R. Fergus, "Depth map prediction from a single image using a multi-scale deep network," *Advances in Neural Information Processing Systems*, vol. 27, pp. 2366–2374, 2014.
- [12] M. Visentini-Scarzanella, T. Sugiura, T. Kaneko, and S. Koto, "Deep monocular 3d reconstruction for assisted navigation in bronchoscopy," *International Journal of Computer-Assisted Radiology and Surgery*, vol. 12, no. 7, pp. 1089–1099, 2017.
- [13] F. Mahmood and N. J. Durr, "Deep learning and conditional random fields-based depth estimation and topographical reconstruction from conventional endoscopy," *Medical image analysis*, vol. 48, pp. 230–243, 2018.
- [14] F. Mahmood, R. Chen, and N. J. Durr, "Unsupervised reverse domain adaptation for synthetic medical images via adversarial training," *IEEE Transactions on Medical Imaging*, vol. 37, no. 12, pp. 2572–2581, 2018.
- [15] T. Zhou, M. Brown, N. Snavely, and D. G. Lowe, "Unsupervised learning of depth and ego-motion from video," in *Proceedings of the IEEE Conference on Computer Vision and Pattern Recognition*, pp. 1851–1858, 2017.
- [16] C. Godard, O. Mac Aodha, and G. J. Brostow, "Unsupervised monocular depth estimation with left-right consistency," in *Proceedings of the IEEE Conference on Computer Vision and Pattern Recognition*, pp. 270–279, 2017.
- [17] S. Shao, Z. Pei, W. Chen, B. Zhang, X. Wu, D. Sun, and D. Doermann, "Self-supervised learning for monocular depth estimation on minimally invasive surgery scenes," in *2021 IEEE International Conference on Robotics and Automation*, pp. 7159–7165, IEEE, 2021.
- [18] R. Wang, S. M. Pizer, and J.-M. Frahm, "Recurrent neural network for (un-) supervised learning of monocular video visual odometry and depth," in *Proceedings of the IEEE Conference on Computer Vision and Pattern Recognition*, pp. 5555–5564, 2019.
- [19] H. Zhang, C. Shen, Y. Li, Y. Cao, Y. Liu, and Y. Yan, "Exploiting temporal consistency for real-time video depth estimation," in *Proceedings of the IEEE International Conference on Computer Vision*, pp. 1725–1734, 2019.
- [20] V. Patil, W. Van Gansbeke, D. Dai, and L. Van Gool, "Don't forget the past: Recurrent depth estimation from monocular video," *IEEE Robotics and Automation Letters*, vol. 5, no. 4, pp. 6813–6820, 2020.
- [21] C. Liu, J. Gu, K. Kim, S. G. Narasimhan, and J. Kautz, "Neural rgb (r) d sensing: Depth and uncertainty from a video camera," in *Proceedings of the IEEE Conference on Computer Vision and Pattern Recognition*, pp. 10986–10995, 2019.
- [22] F. Wimbauer, N. Yang, L. Von Stumberg, N. Zeller, and D. Cremers, "Monorec: Semi-supervised dense reconstruction in dynamic environments from a single moving camera," in *Proceedings of the IEEE Conference on Computer Vision and Pattern Recognition*, pp. 6112–6122, 2021.
- [23] J. Watson, O. Mac Aodha, V. Prisacariu, G. Brostow, and M. Firman, "The temporal opportunist: Self-supervised multi-frame monocular depth," in *Proceedings of the IEEE Conference on Computer Vision and Pattern Recognition*, pp. 1164–1174, 2021.
- [24] M. Jaderberg, K. Simonyan, A. Zisserman, *et al.*, "Spatial transformer networks," in *Advances in Neural Information Processing Systems*, pp. 2017–2025, 2015.
- [25] Z. Wang, A. C. Bovik, H. R. Sheikh, and E. P. Simoncelli, "Image quality assessment: from error visibility to structural similarity," *IEEE Transactions on Image Processing*, vol. 13, no. 4, pp. 600–612, 2004.
- [26] R. T. Collins, "A space-sweep approach to true multi-image matching," in *Proceedings of the IEEE Conference on Computer Vision and Pattern Recognition*, pp. 358–363, IEEE, 1996.
- [27] A. Dosovitskiy, P. Fischer, E. Ilg, P. Hausser, C. Hazirbas, V. Golkov, P. Van Der Smagt, D. Cremers, and T. Brox, "Flownet: Learning optical flow with convolutional networks," in *Proceedings of the IEEE International Conference on Computer Vision*, pp. 2758–2766, 2015.
- [28] J. Dai, H. Qi, Y. Xiong, Y. Li, G. Zhang, H. Hu, and Y. Wei, "Deformable convolutional networks," in *Proceedings of the IEEE International Conference on Computer Vision*, pp. 764–773, 2017.
- [29] C. Godard, O. Mac Aodha, M. Firman, and G. J. Brostow, "Digging into self-supervised monocular depth estimation," in *Proceedings of the IEEE International Conference on Computer Vision*, pp. 3828–3838, 2019.
- [30] D.-A. Clevert, T. Unterthiner, and S. Hochreiter, "Fast and accurate deep network learning by exponential linear units (elus)," *arXiv preprint arXiv:1511.07289*, 2015.
- [31] D. Recasens, J. Lamarca, J. M. Fácil, J. Montiel, and J. Civera, "Endo-depth-and-motion: Reconstruction and tracking in endoscopic videos using depth networks and photometric constraints," *IEEE Robotics and Automation Letters*, vol. 6, no. 4, pp. 7225–7232, 2021.
- [32] A. Geiger, M. Roser, and R. Urtasun, "Efficient large-scale stereo matching," in *Proceedings of the Asian Conference on Computer Vision*, pp. 25–38, Springer, 2010.
- [33] A. Paszke, S. Gross, S. Chintala, G. Chanan, E. Yang, Z. DeVito, Z. Lin, A. Desmaison, L. Antiga, and A. Lerer, "Automatic differentiation in pytorch," 2017.
- [34] D. P. Kingma and J. Ba, "Adam: A method for stochastic optimization," *arXiv preprint arXiv:1412.6980*, 2014.
- [35] J. Deng, W. Dong, R. Socher, L.-J. Li, K. Li, and L. Fei-Fei, "Imagenet: A large-scale hierarchical image database," in *Proceedings of the IEEE Conference on Computer Vision and Pattern Recognition*, pp. 248–255, Ieee, 2009.
- [36] J. Spencer, R. Bowden, and S. Hadfield, "Defeat-net: General monocular depth via simultaneous unsupervised representation learning," in *Proceedings of the IEEE Conference on Computer Vision and Pattern Recognition*, pp. 14402–14413, 2020.